MODELLING OF IN SITU SILICA PARTICLE GROWTH AND DEPOSITION UNDER GEOTHERMAL CONDITIONS

Shuying Chen[1], Kevin Brown[2], and Mark Jermy[1]

[1] Department of Mechanical Engineering, University of Canterbury, Christchurch 8041, New Zealand

[2] GEOKEM, P.O. Box 30-125, Barrington, Christchurch, New Zealand

jasonchen1212@hotmail.com

Keywords: *Reactive transport, silica scaling, amorphous silica deposition.*

ABSTRACT

When cooled geothermal brine is reinjected, colloidal silica may form, deposit, and eventually block the fluid pathways in the aquifer, reducing injectivity. Models of silica deposition, the formation of colloidal silica, especially the growth of silica nanoparticles over time, are of value in the prediction of geothermal well lifetime and the effects of brine treatments and workovers. This paper deals with the transport of silica colloids, once formed.

A 2D Eulerian model to predict the in situ deposition rate of silica is proposed. The driving mechanisms of silica transport considered in the model are diffusion and convection (Levich 1962), and five external forces acting on individual suspended silica nanoparticles: gravity, buoyancy, London-van der Waals force, electrostatic force. The Saffman lift force is shown to be negligible. The modelling results are compared to the observations of Mroczek et al. 2017, in experiments with natural brines in which colloidal silica deposition is suppressed by ageing the brine.

1. INTRODUCTION

Concentrated geothermal fluid is often injected back to the underground to maintain reservoir pressure and sequester toxic minerals. The decrement in amorphous silica solubility due to loss of heat and the increment in concentration due to loss of water may cause silica scaling, which plugs the fluid pathways and gradually reduces the injectivity.

Under typical geothermal conditions, silica scaling may be dominated by the deposition of colloidal silica (Brown 2011). On the other hand, the direct deposition from the dissolved silica (commonly known as molecular deposition) cannot be ignored as well, as there may be a period near the inlet of the fluid path where significant concentrations of dissolved monomeric (molecular) silica coexists with colloidal silica in the fresh (unaged) injectate. From the perspective of the authors of the present work, the deposition process can be described as follows: monomeric silica may firstly polymerise to form nuclei which grow to become colloidal particles, which coat the fracture surfaces (to at least one particle thick) in a time much less than the lifetime of the well. Hence, one can treat the wall as having the electrochemical properties of silica, regardless of rock mineral content, i.e. the deposition is recognised as the interaction between deposited and suspended silica particles.

Before looking into the transport of the silica particles, it is necessary to understand the hydrodynamics of the injecting process first. A simple idealised model was proposed in the previous workshop (Chen et al. 2017), shown in Figure 1.

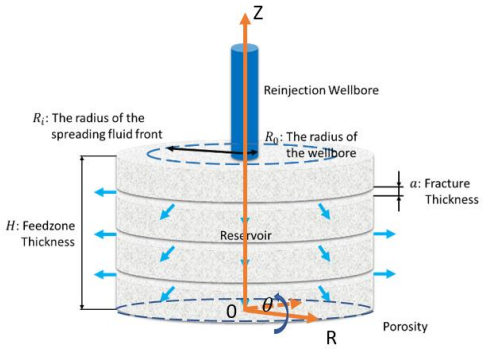

Figure 1: Simplified geometry consisting of an injection wellbore and geothermal reservoir.

The blue cylinder in Fig. 1 represents the injection wellbore, which is assumed to fully penetrate the domain. The cooled and condensed geothermal fluid is reinjected through the wellbore at the mass flow rate $\dot{m}$, and is assumed to uniformly spread along horizontal fracture networks, which are homogeneously distributed (i.e. equally spaced) in the vertical direction. Therefore, the geometry is axis-symmetric with radial distance R from the wellbore. The reservoir is assumed both vertically and horizontally homogeneous, i.e. rock properties are constant over a certain range of depths z between impermeable basements and cap rocks and do not vary with radial distances R. The model is clearly much simpler than real geothermal reservoirs, but serves to study the evolution of the silica.

In a fracture network, there may be preferential flow paths, which make a large contribution to the permeability despite forming a small fraction of the whole porosity. In the case of reinjection, the horizontal fractures are assumed to be the preferential flow paths, though these may account for a relatively small part of the whole porosity. As the width of the fracture is larger than the thickness of the aperture by orders of magnitude, the fracture network is treated as equivalent to two parallel flat plates (shown in Fig. 2). Tortuosity of the fractures is neglected.

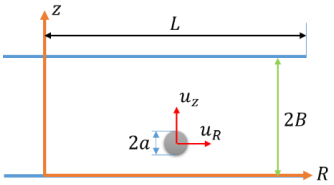

Figure 2: Coordinate set up. The flow is assumed to be fully developed for $R \geq R_0$, where R_0 is the radius of the injection wellbore.

The fracture domain shown in Fig. 2 are $R_0 \leq R \leq R_{max}$ and $0 \leq z \leq B$. However, for the particle transport, since the coordinate represents the centre of the particle, the minimum z is no longer equal to 0 but equal to the radius of the silica particle, i.e. $z = a$, which can be obtained when the particle touches the plate. Hence, the domain for colloidal silica transport is $R_0 \leq R \leq R_{max}$ and $a \leq z \leq B$.

There are five external forces in the vertical (i.e. z) direction, which are recognised to have effects on the silica particle transport: gravity, buoyancy, Saffman lift force, London-van der Waals' force, and electrostatic force, shown in the figure below.

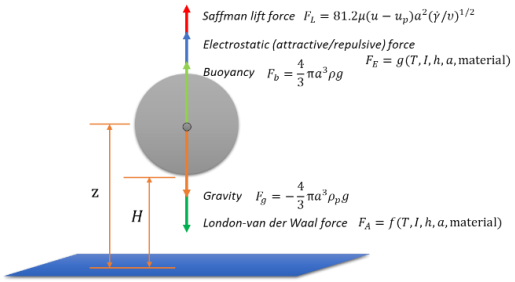

Figure 3: five external forces of interest applied on the colloidal silica particle

1. Gravity and buoyancy

By coupling the expressions for gravity and buoyancy, the net gravity F_g can be described as:

$$F_g = -\frac{4}{3}\pi a^3(\rho_p - \rho)g \tag{1}$$

where ρ_p is the density of amorphous silica, and g is the gravitational acceleration.

2. Saffman lift force

The Saffman lift force, F_L, is a lift force experienced by a sphere transporting through a viscous liquid perpendicular to the flow direction due to the velocity difference (Saffman 1964). It can be defined by:

$$F_L = 81.2\mu(u_{fR} - u_R)a^2(\dot{\gamma}/\upsilon)^{1/2} \tag{2}$$

where $(u_{fR} - u_R)$ represents the velocity difference between the flow and the particle of interest, i.e. the relative velocity, and $\dot{\gamma} = \frac{\partial u}{\partial z} = -3u_m\frac{(z-B)}{B^2}$ is the shear rate: u_m is the mean velocity of the fluid flow (equivalent to u_{Rm} defined in Eq. 24), and B is the half of the distance of between the two plates shown in Fig. 2.

3. London-van der Waals' force

The London-van der Waals' force F_A exists among any pair of objects, which can be expressed by:

$$F_A = \frac{dV_A}{dH} \tag{3}$$

where H is the separation distance (i.e. the shortest distance between two objects), and V_A is the attractive potential due to the London-van der Waals' force. In the case of two spherical particles 1 and 2 having the radii a_1 and a_2 respectively, it is defined by (Hamaker 1937):

$$V_A = -\frac{A}{6}\left(\frac{2a_1a_2}{H^2 + 2H(a_1+a_2)} + \frac{2a_1a_2}{(H+2a_1)(H+2a_2)} + \ln\left[\frac{H^2+2H(a_1+a_2)}{(H+2a_1)(H+2a_2)}\right]\right) \tag{4}$$

where A is the Hamaker constant, represented by Eq. 5 below (Hamaker 1937, London 1937):

$$A = 0.75k_BT(1+2\kappa H)e^{-2\kappa H} + \frac{3\hbar\omega}{16\sqrt{2}}\frac{(n_1^2-n_3^2)^2}{(n_1^2+n_3^2)^{3/2}}\left[1+\left(\frac{H}{\lambda}\right)^q\right]^{-1/q} \tag{5}$$

where, $\kappa = \sqrt{\frac{2e^2N_Ac_iz^2}{\varepsilon k_BT}}$ is the Debye-Huckel parameter, e is the electron charge, N_A is Avogadro's number, c_i is the concentration of the background electrolyte, z is the valence of the electrolyte, ε is the permittivity, $\hbar$ is the Planck constant divided by 2π, $\lambda = \frac{c}{\pi^2\omega}\sqrt{\frac{2}{n_3^2(n_1^2+n_3^2)}}$ is the characteristic wavelength of the retardation effect, c is the speed of light, $\omega = 3.3 \times 10^{15}$ is the characteristic frequency of the retardation effect, $n_1 = 1.43$ and $n_2 = 1.33$ are the refractive index of silica and medium (water) respectively, and $q = 1.185$ is a fitting factor (Škvarla 2013).

As described before, the silica deposition problem near the fracture surface is simplified to the interactions between suspended silica particles and amorphous silica coated plates. Thus, in the present work, a_1 can be defined as the averaged radius of the formed silica colloids, and a_2 may be defined using any convenient value that satisfies $a_2 \gg a_1$. The interaction between suspended particles themselves is included in the aggregation model described in a separate paper in these proceedings.

4. Electrostatic force

The electrostatic repulsion force between two similar colloids is due to the surface charge φ_0. In the case of amorphous silica, the silanol group may either dissociate a proton to the solution or obtains a proton from the solution depending on the pH. Hence, the surface of a silica particle will be either negatively or positively charged unless the pH is at the "point of zero charge" where these effects are balanced.

Ions from the background electrolyte are adsorbed to the charged surface to form a charged layer, called the Stern layer or the first layer. Due to the existence of the first layer, ions with opposite charge are attracted and electrically mask the first layer. These ions form another charged layer, called the second layer or the diffuse layer since it is loosely organized. The assembly comprising the two charged layers is named the "double layer" or "electrical double layer".

Similarly, the electrostatic force, F_E can be derived using the electrostatic potential energy V_E,:

$$F_E = \frac{dV_E}{dH} \tag{6}$$

In the frame of DLVO theory (Deraguin and Landau 1941, Verwey and Overbeek 1955), which is commonly used to quantitatively describe the interaction between colloids, the

electrostatic repulsion potential can be expressed as Eq. 7 below by assuming the surface potential is maintained constant (Derjaguin 1940):

$$V_E = 2\pi\varepsilon\varphi_0{}^2 r \ln[1 + \exp(-\kappa h)] \quad (7)$$

In practice, another parameter – the zeta-potential (or ζ-potential) is usually substituted in place of surface potential φ_0 in Eq. 7, which may be smaller than φ_0 in absolute value but is easier to be estimated by measuring the mobility of the colloids in an electric field. It has been shown that DLVO theory can predict the stability of colloids of a range of chemical compositions with reasonable accuracy (Adamczyk and Weroński 1999). However, amorphous silica is an exception (Iler 1979, De Gennes 1987, Healy 1994, Kobayashi et al. 2005). In another paper by the present authors in these proceedings, it is proved that Ohshima's latest soft particle model (colloidal particles that are coated by ion-penetrable surface layers of polyelectrolytes, as shown in Fig. 4 below) (Ohshima 2015) can be used to explain the unexpected interaction behaviours at pH = 4, 6, and 8 and $c_{KCl} = 0.001 - 1$M at 25℃, which may offer a better understanding of the mechanisms for silica particle attachment and silica scaling, at least at room temperature.

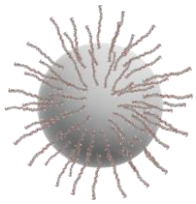

Figure 4: A sketch of a colloidal particle with a hairy layer, the "hairs" being polymer chains of silicone.

According to Ohshima (2015), the electrostatic force due to the unique effects of the ion-penetrable surface layers (or the hairy layers) $F_{E,sp}$ can be described by:

$$F_{E,sp} = \frac{2\pi a_1 a_2}{a_1 + a_2} 64 c_i N_A k_B T \tanh\left(\frac{y_1}{4}\right) \tanh\left(\frac{y_2}{4}\right) \exp[-\kappa(H - d_1 - d_2)] \quad (8)$$

where d_1 and d_2 are the thickness of the hairy layers of particle 1 and 2 respectively, and y_1 and y_2 are defined below:

$$y_1 = \text{arcsinh}\left(\frac{Z_1 N_1}{2zn}\right) - \tanh\left[\frac{\text{arcsinh}\left(\frac{Z_1 N_1}{2zn}\right)}{2}\right] \quad (9)$$

$$y_2 = \text{arcsinh}\left(\frac{Z_2 N_2}{zn}\right) - \tanh\left[\frac{\text{arcsinh}\left(\frac{Z_2 N_2}{zn}\right)}{2}\right] \quad (10)$$

where Z_1, Z_2 and N_1, N_2 are the valence and the number density of the dissociated groups within the hairy layers of the particle 1 and 2 respectively, n is the number concentration of the background electrolyte. When the physical and chemical conditions are fixed, it is reasonable to assume that the surface charge density σ_0 is a constant, which can be estimated by following (Sonnefeld 1995) and the hairy layers of the particle 1 and 2 are charged at the uniform charge densities ρ_{fix1} and ρ_{fix2} separately. Hence, the correlation between Z, N, and σ_0 can be expressed:

$$\rho_{fix1} = Z_1 e N_1 = \sigma_0 / d_1 \quad (11)$$

$$\rho_{fix2} = Z_2 e N_2 = \sigma_0 / d_2 \quad (12)$$

Therefore, the total external force F applied on a suspended silica nanoparticle can be defined by:

In the frame of the DLVO theory:

$$F = F_g + F_L + F_A + F_E \quad (13)$$

Alternatively, applying the soft particle model:

$$F = F_g + F_L + F_A + F_{E,sp} \quad (14)$$

As described in another paper by the present authors in these proceedings, compared to Eq. 7, Eq. 8 has been proved more suitable to model the interactions between colloidal silica particles. Therefore, only Eq. 14 is considered in the present work.

2. MATHEMATICAL SCHEME

2.1 Hydrodynamics

The hydrodynamics sub-model is used to find the velocity at which the fluid travels away from the wellbore, within the fractures. To study the hydrodynamics, consider the mass continuity equation first:

$$\frac{\partial \rho}{\partial t} + \nabla \cdot \boldsymbol{j} = 0 \quad (15)$$

where ρ is the density of the injectate, which is assumed to be equal to that of water under the same physical conditions, $\nabla \cdot$ is the divergence, $\boldsymbol{j}$ is the mass flux vector, and the term $\nabla \cdot \boldsymbol{j}$ is equal to $\frac{1}{R}\frac{\partial(R \cdot j_R)}{\partial r} + \frac{1}{R}\frac{\partial j_\theta}{\partial \theta} + \frac{\partial j_z}{\partial z}$ for cylindrical coordinates.

As the density of water changes modestly (e.g. decreasing by approximately 15.6% on heating from 952.8 kg m^{-3} at 155 ℃ to 803.7 kg m^{-3} 260 ℃ under 20 MPa (Keenan 1978)), there will be a flux from cell to cell as the water heats up, which can be modelled as a pressure, or as a volume flux due to change in volume. Since the volume flux is usually very small compared to the other fluxes, for simplicity, it may be reasonably assumed that the fluid is incompressible, i.e. $\frac{\partial \rho}{\partial t} = 0$. Hence, the mass continuity equation can be simplified to Eq. 16 below:

$$\nabla \cdot \boldsymbol{j} = 0 \quad (16)$$

Eq. 16 is equivalent to the following expression for cylindrical coordinates:

$$\frac{1}{R}\frac{\partial(R \cdot j_R)}{\partial R} + \frac{1}{R}\frac{\partial j_\theta}{\partial \theta} + \frac{\partial j_z}{\partial z} = 0 \quad (17)$$

The permeability of the rock between the adjacent fractures is assumed to be zero, i.e. no fluid can flow vertically through the rock even under the effect of an infinitely high pressure gradient. In practice, there will be vertical fractures, but with small or zero pressure gradient in the vertical direction, there will be little vertical flow. Gravitational flow is neglected. Hence there is no mass transfer of the injectate in the z-axis, i.e. $j_z = 0$. Since the geometry is axis-symmetrical there is no tangential flow. The fractures are assumed to be vertically

homogenously distributed. Hence Eq. 18 and 19 can be obtained:

$$\frac{\partial j_\theta}{\partial \theta} = 0 \tag{18}$$

$$\frac{\partial j_z}{\partial z} = 0 \tag{19}$$

Eq. 17 can be simplified to:

$$\frac{1}{R}\frac{\partial (R \cdot j_r)}{\partial R} = 0 \tag{20}$$

The radial Navier-Stokes momentum equation for the two-dimensional incompressible flow is:

$$\begin{aligned} &\rho\left(u_R\frac{\partial u_R}{\partial R} + u_z\frac{\partial u_z}{\partial z}\right) \\ &= -\frac{\partial p}{\partial R} + \rho g_R \\ &+ \mu\left\{\frac{\partial}{\partial R}\left[\frac{1}{R}\frac{\partial}{\partial R}(Ru_R)\right] + \frac{\partial^2 u_z}{\partial z^2}\right\} \end{aligned} \tag{21}$$

where u_z is the velocity of the fluid in the z-axis, $\frac{\partial p}{\partial R}$ is the pressure gradient, which physically drives the flows, g_R is the gravitational acceleration with respect to the radial direction, which is zero, and μ is the dynamic viscosity of the fluid. The flow is laminar as in practice the Reynolds number is small.

Since $u_z = 0$ and $g_R = 0$, Eq. 21 can be simplified to:

$$\mu\frac{\partial^2 u_R}{\partial R^2} = \frac{\partial p}{\partial R} \tag{22}$$

According to the no-slip boundary condition: $u_R = 0$ when $R = 0$ and $R = 2B$, the solution to Eq. 22 can be obtained by integrating twice:

$$u_R(z) = -\frac{dp}{dx}\frac{B^2}{2\mu}\left(1 - \frac{(z-B)^2}{B^2}\right) \tag{23}$$

i.e. a parabolic velocity profile of the Poiseuille type, where the maximum velocity $u_{Rmax} = -\frac{dp}{dx}\frac{B^2}{2\mu}$ occurs when $z = B$.

The average velocity u_{Rm}, can be expressed with respect to the maximum velocity u_{Rmax}:

$$\begin{aligned} u_{Rm} &= \frac{\dot{Q}}{A} = \frac{1}{A}\int u_R\, dA \\ &= \frac{1}{b(2B)}\int_0^{2B} u_{Rmax}\left(1 - \frac{(z-B)^2}{B^2}\right) b\, dz \\ &= \frac{2}{3}u_{Rmax} \end{aligned} \tag{24}$$

where *b* is the width of the fracture.

Hence, when the no-slip condition applies, the velocity profile can be eventually represented as:

for $0 \le z \le B$,

$$u_R(z) = \frac{3}{2}u_{Rm}\left(1 - \frac{(z-B)^2}{B^2}\right) \tag{25}$$

2.2 Governing equation for particle transport

It is desired to predict particle transport from fluid to collector under the influence of external forces $\boldsymbol{F}$ (i.e. $F_R, F_\theta,$ and F_z). Hence, by coupling the continuity and the transport equations, one can obtain the governing equation for particle transport:

$$\begin{aligned} \frac{\partial C_{ps}}{\partial t} + \nabla\cdot\left(\boldsymbol{u}C_{ps}\right) + \nabla\cdot\left(\frac{\boldsymbol{D}\boldsymbol{F}C_{ps}}{k_BT}\right) \\ = \nabla\cdot\left(\boldsymbol{D}\nabla C_{ps}\right) + S_{ps} \end{aligned} \tag{26}$$

which is equivalent to:

$$\begin{aligned} &\frac{\partial C_{ps}}{\partial t} + \frac{1}{R}\frac{\partial}{\partial R}\left(Ru_RC_{ps}\right) + \frac{1}{R}\frac{\partial}{\partial \theta}\left(u_\theta C_{ps}\right) \\ &+ \frac{\partial}{\partial z}\left(u_zC_{ps}\right) + \frac{1}{R}\frac{\partial}{\partial R}\left(R\frac{D_RF_RC_{ps}}{k_BT}\right) \\ &+ \frac{1}{r}\frac{\partial}{\partial \theta}\left(\frac{D_\theta F_\theta C_{ps}}{k_BT}\right) + \frac{\partial}{\partial z}\left(\frac{D_zF_zC_{ps}}{k_BT}\right) \\ &= \frac{1}{R}\frac{\partial}{\partial R}\left(D_RR\frac{\partial C_{ps}}{\partial R}\right) + \frac{1}{R^2}\frac{\partial}{\partial \theta}\left(D_\theta\frac{\partial C_{ps}}{\partial \theta}\right) \\ &+ \frac{\partial}{\partial z}\left(D_z\frac{\partial C_{ps}}{\partial z}\right) + S_{ps} \end{aligned} \tag{27}$$

where C_{ps} is the concentration of the particles of interest (the subscript ps stands for "polymerised silica"); k_B is the Boltzmann constant; T is the absolute temperature; R, θ, and z are the spatial coordinates of the centre of the particles; $\boldsymbol{u}$ (i.e. $u_R, u_\theta,$ and u_z) is the particle transporting velocities induced by the fluid, $\boldsymbol{D}$ (i.e. $D_R, D_\theta,$ and D_z) is the diffusion coefficient of the particles, $\boldsymbol{F}$ (i.e. $F_R, F_\theta,$ and F_z) is the net external force acting on a particle, corresponding to the directions of $R, \theta,$ and z respectively; and S_{ps} is the source or sink term, representing the quantity of particles generated or lost in per unit volume and time.

By assuming the particle velocities induced by flow in the R, θ, and z directions are equal to the fluid velocity:

$$u_R = u_{fR} = \frac{3}{2}u_m\left(1 - \frac{(z-B)^2}{B^2}\right) \tag{28}$$

$$u_\theta = u_{f\theta} = 0 \tag{29}$$

$$u_z = u_{fz} = 0 \tag{30}$$

Therefore, according to Eq. 2 and 28, the Saffman lift force becomes zero.

By assuming the diffusion coefficients of the particles in the R, θ, and z directions are equal and can be expressed using the Stokes-Einstein equation (Eq. 31):

$$D_R = D_\theta = D_z = D = \frac{k_BT}{6\pi\mu a} \tag{31}$$

where a is the particle radius.

As described previously, it is assumed that there is no external force acting on the particles in the R and θ directions (i.e. $F_R = 0$ and $F_\theta = 0$), therefore:

$$F_z = F \tag{32}$$

By assuming there is no concentration gradient of the particles in the θ directions as the model is axis-symmetrical:

$$\frac{\partial C}{\partial \theta} = 0 \quad (33)$$

Therefore, the governing equation Eq. 27 can be simplified to:

$$\frac{\partial C_{ps}}{\partial t} + \frac{1}{R}\frac{\partial}{\partial R}\left(Ru_R C_{ps}\right) + \frac{\partial}{\partial z}\left(\frac{DF_z C_{ps}}{k_B T}\right) = \frac{1}{R}\frac{\partial}{\partial R}\left(DR\frac{\partial C_{ps}}{\partial R}\right) + \frac{\partial}{\partial z}\left(D\frac{\partial C_{ps}}{\partial z}\right) + S_{ps} \quad (34)$$

To solve Eq. 34, it is necessary to define the boundary conditions. In the radial (R) direction, the boundary conditions for polymerised silica transport can be defined by:

$$C_{ps}|_{R=R_0} = c_{\text{inj}}^{\text{ps}} \quad (35)$$

$$\frac{\partial C_{ps}}{\partial R}|_{R=R_{max}} = 0 \quad (36)$$

Eq. 36 indicates that the concentration of the silica particles at the entrance of the fractures is a constant; and Eq. 37 states that the concentration gradient is zero at the far end of the fracture, which models the far end as the "outlet" of the injectate pathway.

Since the geometry is symmetrical with respect to $z = B$ (as shown in Fig. 2), Eq. 37 can be defined below:

$$\frac{\partial C_{ps}}{\partial R}|_{z=B} = 0 \quad (37)$$

Eq. 37 physically means that the concentration gradient at $z = B$ is zero due to the symmetry, i.e. the properties at $\mathrm{B} + \mathrm{dz}/2$ and $\mathrm{B} - \mathrm{dz}/2$ are equal.

As the conditions near the fracture surface (or, more conventionally, the collector) are still not well understood, defining the boundary conditions at $z = a$ is more complex. The following two models consider two different cases:

1. The perfect-sink model

This assumes that the particles immediately deposit and irreversibly disappear from the brine system once they reach the rock surface. Within a fracture, the following boundary condition can be found:

$$C_{ps}|_{z=a} = 0 \quad (38)$$

The perfect-sink model does not consider the formation of the deposition as an independent phase on the solid surface, i.e. it does not reveal the possibility of immobilisation (i.e. attachment and deposition) followed by detachment. However in practice, when particles reach the collector, some of them may attach and deposit permanently but the rest of them may not; and the immobilised particles could be released from the collector as well. Nevertheless, in the case of geothermal reinjection, the perfect-sink model may be used to study the initial attachment between suspended colloidal silica particles and "clean" fracture surfaces.

2. The non-penetration model

This model (Adamczyk and Van de Ven 1984) considers that the normal flux of particles near the collector surface converges to zero and a source term is added to the governing equations to model the processes that cannot be expressed explicitly yet, i.e.:

$$j_z = 0 \text{ when } z = a \quad (39)$$

which is equivalent to:

$$\frac{\partial C_{ps}}{\partial R}|_{z=a} = 0 \quad (40)$$

The hybrid difference scheme (Spalding 1972) is used to solve the governing equations. As there are two assumptions regarding the boundary conditions, there are two cases to be compared and discussed.

2.3 In situ silica polymerisation and particle growth

The silica scaling model proposed in the present work also couples two sub-models of silica chemistry: in situ silica polymerisation (from dissolved silica) and subsequent particle growth. These two sub-models can be used to predict the local concentration of polymerised silica and the averaged particle size under known conditions. The former sub-model is developed by following (Weres et al. 1981), which can predict the silica polymerisation curve over time but is unable to predict the size of formed silica nanoparticles; and the later one is described in another paper by the present authors in this these proceedings, which adopts the Lifshitz-Slyozov-Wagner (LSW) theory to estimate the silica particle size over time.

2.4 Immobilisation of deposited silica particles

No matter whichever model (Eq. 38 or 40) is chosen for the boundary condition at $z = a$, it can be expected that the colloidal silica becomes immobilised and a part of the collector (i.e. the fracture surface coated with amorphous silica).

Hence, at $z = a$, the parameters, such as the diffusion coefficient D, the convection induced by the flow u_R, the external force F, and the source/sink term S_{ps}, that have effects on the particle transport should be set to zero.

3. VALIDATION: MROCZEK ET AL'S OHAAKI RAPID COOLING SCALING TRIAL

Mroczek et al. (2013; 2017) experimentally studied the silica scaling potential of cooled geothermal water saturated with amorphous silica at the Wairakei and Ohaaki fields, New Zealand. Small-scale field experiments at the Wairakei field, had shown a low silica scaling rate after brine (containing 730 ppm silica) was cooled to 30 ℃ and aged for several days before reinjection. Due to this success, the first major large-scale injection of cold (30 ℃) geothermal water in New Zealand was carried out at the Wairakei field. Mroczek et al. 2017 reported that, after a 10-month trial, there was no evidence of any reduction in the performance of the reinjection (i.e. the injectivity) due to silica scaling. However, in a similar small-scale field investigation at Ohaaki, silica deposition was observed in a rapidly cooled, but only briefly aged (30 min at 80 ℃) brine containing 840 ppm dissolved and polymerised silica. Hence no large-scale field trial at Ohaaki was proposed.

Although the idealised geothermal reservoir defined in the present work (Fig. 1 and 2) differs in geometry from the scaling rig (see Fig. 1 in Mroczek et al. 2017), it is still possible to compare and validate whether the model proposed in the present work can reasonably estimate the

silica deposition rate under known conditions, and predict the possible results of any future field trial.

3.1 Inputs

Based on the descriptions and Table 1-3 of Mroczek et al. 2017, the inputs required for the present work are summarised in Table 1 below:

Table 1: Summary of input parameters.

Input parameter	In Mroczek et al. 2017	In the present work
Radius of injection wellbore	-	0.122 m
Thickness of feedzone	-	120 m
Initial fracture aperture	-	0.002 m
Initial reservoir porosity	-	0.01
Initial fracture porosity	-	1
Initial permeability of fractures	-	5.0×10^{-12} m^2
Injecting mass flow rate	27 L/min	270 t/hr
Temperature	~80 ℃	80 ℃
pH	5.69	5.69
Ionic strength	~0.043 M	0.043 M
Initial concentration of dissolved silica	849 ppm	849 ppm
Injection time	46 days	40 minutes

3.2 Modelling results

To compare the model predictions to Mroczek et al.'s (2017) small-scale field experiment at Ohaaki, results are compared at points in the model which have the same residence time (i.e. how long it takes the injectate to transport from the inlet to a point of interest), as the sampling points T1, T2, T3, T4, B2, and B6 in Mroczek et al.'s trial. For example, the residence time 6.3 minutes at $R = 366.23$ m in the present model is equal to that of T1 in Mroczek et al. 2017.

Since (1) the given maximum residence time of the sampling points in the Ohaaki small-scale field experiment is about 30 minutes at B6, (2) only the estimation of the deposition rates are of interest in the present work, and (3) the effects of decreasing injectivity on the fluid flow are not taken into consideration in the model, to minimise the computational cost while maintaining the accuracy of the computed results, a relatively short injection time of 40 minutes, which covers the residence times of all measurements, is used.

3.2.1 Perfect-sink model vs. non-penetration model

Use of the perfect-sink model predicted a deposition rate at least 12 orders of magnitude higher than the observations. The non-penetration model (Eq. 40) predicted a deposition rate of the correct order of magnitude, so was used for all the results shown below.

3.2.2 In situ concentration of dissolved silica

The concentration distribution of the dissolved silica is shown in Fig. 5 below:

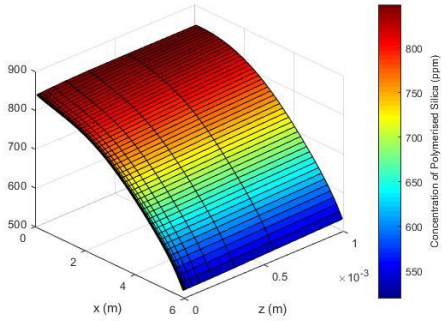

Figure 5: Dissolved silica concentration distribution, where $x = R - R_0$ (i.e. the injection wellbore is not included in the domain).

The concentration of the dissolved silica is expected to drop along with both the radial and the vertical directions due to polymerisation and molecular deposition. According to the Fig. 5 above, the decrease near the fracture surface is much smaller than the decline along the fluid pathway, suggesting that the silica polymerisation is the main reason for the loss of dissolved silica.

The comparison between the observed and predicted dissolved silica concentration at the sampling points is shown in Fig. 6 below:

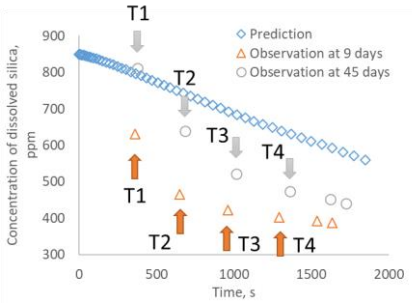

Figure 6: Comparison between the observed (reproduced from Mroczek et al. 2017) and the predicted in situ concentration of the dissolved silica, where T1-T4 are the sampling points.

The model predicts a reduction in the dissolved silica concentration of the correct order of magnitude, and is in closer agreement with the 45-day observations than the 9-day observations. The predictions have a lower rate of decline (slope) than the 45-day observations by a factor of approximately two. The silica polymerisation model of Weres et al. (1981) takes the effects of sodium chloride into account, but not other ions e.g. Mg^{2+}, Al^{3+}, Br^{-}, SO_4^{2-}, which are expected to be present in the trials. Weres et al. (1981) qualitatively reported, but did not quantify, the accelerating effects of larger anions on silica polymerisation.

3.2.3 In situ silica particle size

Mroczek et al. (2017) reported that, at the T4 (~22.1 min after injection) and B2 (~26.3 min after injection) sampling points, the average diameter of the formed silica nanoparticles was 8-9 nm.

The proposed model predicts 7.84 nm at the same residence time. This suggests that the silica particle growth sub-model

can reasonably predict the in situ particle size. Reliable prediction of the particle size is essential for predictions of subsequent growth, aggregation and deposition.

3.2.4 In situ concentration of polymerised silica and deposition rate

To differentiate the roles of the molecular and colloidal deposition mechanisms, the concentration distribution of the polymerised (i.e. particulate) and deposited silica due to the molecular and colloidal deposition after 40 minutes of reinjection is separately shown in Fig. 7 (a) and (b) below:

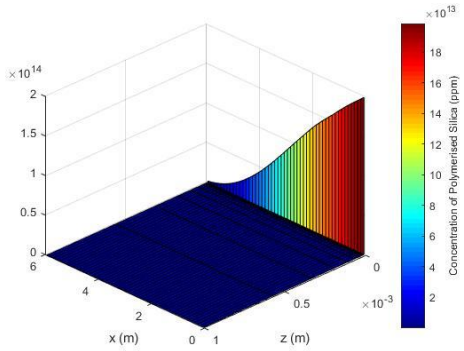

(a)

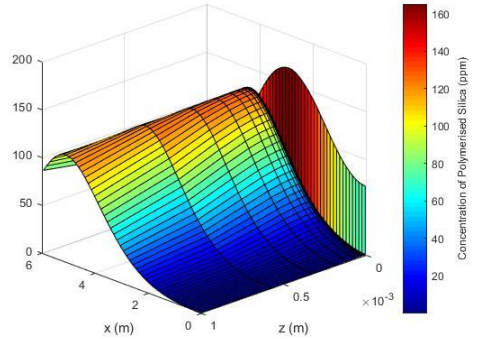

(b)

Figure 7: Concentration distribution of (a) polymerised and deposited silica (molecular and colloidal), (b) polymerised and deposited silica (colloidal only) after 40 minutes of reinjection. The discontinuous values at $z = a \approx 0$ represent the immobilised (deposited) silica scale. In (a), note that the concentration of the suspended silica particles is hindered by the accumulating silica scale.

Based on the results shown in Fig. 7 above, the comparison between the observed and predicted deposition rates at the sampling points is summarised in Table 2 below:

Table 2: Comparison between the observed (at 46 days) and the predicted in situ silica deposition rate ($\mathbf{kg\ m^{-2}\ s^{-1}}$)

Deposition rate at	In Mroczek et al. 2017	Model predictions	Model predictions (colloidal deposition only)
T1	5.07×10^{-9}	5.04×10^{-8}	7.81×10^{-20}
T2	5.23×10^{-8}	3.12×10^{-8}	7.87×10^{-20}
T3	2.38×10^{-8}	1.67×10^{-8}	5.81×10^{-20}
T4	3.17×10^{-9}	5.07×10^{-9}	3.28×10^{-20}

For comparison, the deposition rates of colloidal silica alone (excluding molecular deposition) are shown in the last column of Table 2, which suggests that the molecular deposition is the dominant silica scaling mechanism. Under the conditions summarised in Table 1, the predictions in the third column of Table 2 match the observations to within one order of magnitude. The exception is at T1, where the experimental observations show a rapid rise in deposition rate from T1 to T2. In the model, it occurs that, while the molecular deposition rate constantly decreases from the inlet, the colloidal deposition rate continuously increases from the inlet, reaches its maximum before T2 which is approximately two times higher than the colloidal deposition rate near the inlet, and begins to drop near T2.

Since the effects of ions other than Na^+ and Cl^- on the interactions of colloidal silica are not included in the proposed model yet, the deposition of flocculated (aggregated) colloidal silica due to iron corrosion (Mroczek et al. 2017) is not modelled in the present work. This may have a role in explaining the discrepancy of one order of magnitude between the observation and the prediction at T1.

Despite the discrepancy, the modelling results suggest that the dominant mechanism for silica scaling should be the molecular deposition, and the deposition of colloidal silica in these aged brines may be negligible, which is consistent with Mroczek et al.'s (2017) conclusion, and indeed the aim of their tests was to suppress colloidal deposition.

The low colloidal deposition rate may be due to, on one hand, the relatively small particle size (compared to unaged brines) which leads to a weaker attractive London-van der Waals' force and hence it becomes more difficult for the suspended particles to overcome the repulsive electrostatic force to reach the fracture surface (i.e. deposit), resulting in a negligible deposition rate of colloidal silica in this case; on the other hand, although a considerable amount of the dissolved silica has been consumed rapidly to form silica nanoparticles near the inlet of the fluid pathway, the remaining concentration of dissolved silica is still high enough to yield a considerable molecular deposition rate.

3.2.5 External force

The quantified external forces applied on a single silica nanoparticle are plotted in Fig. 8 below:

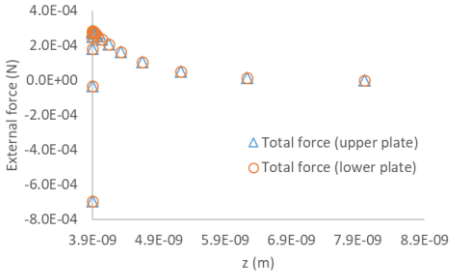

(a)

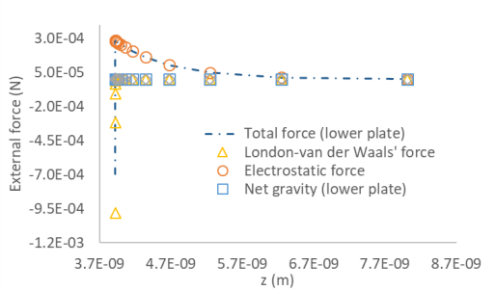

(b)

Figure 8: External forces applied on a single silica particle: (a) comparison between the total forces with respect to the upper and lower plates; (b) comparison among the external forces (the Saffman lift force is zero and excluded for clarity).

The results shown in Fig. 8 (a) indicate that the effect of the net gravity on the transport of silica particle is negligible. Therefore, the problem becomes fully symmetrical with respect to $z = B$. Fig. 8 (b) suggests that, under the conditions shown in Table 1, the coupled effects of London-van der Waals' force and the electrostatic force determine the interactions between the suspended particles and the silica coated fracture surface.

4. CONCLUSION

A silica scaling model, which considers the effects of the externals forces applied on formed silica nanoparticles and in situ silica particle growth is proposed. The validation results suggest that the model may be useful for predicting the in situ silica deposition rate, however the remaining discrepancies may be due to the presence of salts other than sodium chloride, whose effects on the silica polymerisation and the interactions between silica particles are unable to be quantified in the proposed model. The experimental observations used to validate the model are dominated by molecular deposition, and thus are not a stringent test of the colloidal silica transport. Further validation must be done with colloidal-dominated systems.

REFERENCE

Adamczyk, Z. and T. Van de Ven (1984). "Kinetics of particle accumulation at collector surfaces. I. Approximate analytical solutions." Journal of Colloid and Interface Science 97(1): 68-90.

Adamczyk, Z. and P. Weroński (1999). "Application of the DLVO theory for particle deposition problems." Advances in colloid and interface science 83(1-3): 137-226.

Brown, K. (2011). Thermodynamics and kinetics of silica scaling. Proceedings of International Workshop on Mineral Scaling.

Chen, S., et al. (2017). A model of silica colloid growth, stability and transport used to predict geothermal reinjection lifetime. New Zealand Geothermal Workshop 2017, Rotorua, New Zealand.

De Gennes, P. (1987). "Polymers at an interface; a simplified view." Advances in colloid and interface science 27(3-4): 189-209.

Deraguin, B. and L. Landau (1941). "Theory of the stability of strongly charged lyophobic sols and of the adhesion of strongly charged particles in solution of electrolytes." Acta Physicochim: USSR 14: 633-662.

Derjaguin, B. (1940). "On the repulsive forces between charged colloid particles and on the theory of slow coagulation and stability of lyophobe sols." Transactions of the Faraday Society 35: 203-215.

Hamaker, H. (1937). "The London—van der Waals attraction between spherical particles." physica 4(10): 1058-1072.

Healy, T. W. (1994). "Stability of aqueous silica sols." Advances in Chemistry Series 234: 147-147.

Iler, R. K. (1979). "Chemistry of Silica--Solubility, Polymerization, Colloid and Surface Properties, and Biochemistry."

Keenan, J. H. (1978). Steam tables: thermodynamic properties of water including vapour, liquid, and solid phases (International system of units - S.I.). N.Y, Wiley.

Kobayashi, M., et al. (2005). "Aggregation and charging of colloidal silica particles: effect of particle size." Langmuir 21(13): 5761-5769.

Levich, V. G. (1962). "Physicochemical hydrodynamics."

London, F. (1937). "The general theory of molecular forces." Transactions of the Faraday Society 33: 8b-26.

Mroczek, E., et al. (2017). "Silica scaling in cooled silica saturated geothermal water: Comparison between Wairakei and Ohaaki geothermal fields, New Zealand." Geothermics 69: 145-152.

Mroczek, E., et al. (2013). Silica Scaling Trial and Injection of Cold Separated Geothermal Water At Wairakei, New Zealand. 35th New Zealand Geothermal Workshop, number November.

Ohshima, H. (2015). "Electrostatic interaction of soft particles." Advances in colloid and interface science 226: 2-16.

Saffman, P. (1964). "The amplification of a weak magnetic field by turbulent motion of a fluid of large conductivity." Journal of Fluid Mechanics 18(3): 449-465.

Škvarla, J. i. (2013). "Quantitative interpretation of anomalous coagulation behavior of colloidal silica using a swellable polyelectrolyte gel model of electrical double layer." Langmuir 29(28): 8809-8824.

Sonnefeld, J. (1995). "Surface charge density on spherical silica particles in aqueous alkali chloride solutions." Colloid and polymer science 273(10): 932-938.

Spalding, D. B. (1972). "A novel finite difference formulation for differential expressions involving both first and second derivatives." International Journal for Numerical Methods in Engineering 4(4): 551-559.

Verwey, E. J. W. and J. T. G. Overbeek (1955). "Theory of the stability of lyophobic colloids." Journal of Colloid Science 10(2): 224-225.

Weres, O., et al. (1981). "Kinetics of silica polymerization." Journal of Colloid and Interface Science 84(2): 379-402.